High-energy collective electronic excitations in free-standing single-layer graphene

P. Wachsmuth,[1,*] R. Hambach,[1] M. K. Kinyanjui,[1] M. Guzzo,[2,†] G. Benner,[3] and U. Kaiser[1]
[1]*Electron Microscopy Group of Materials Science, Ulm University, Albert-Einstein-Allee 11, 89081 Ulm, Germany*
[2]*Laboratoire des Solides Irradiés, Ecole Polytechnique, CNRS, CEA-DSM, F-91128 Palaiseau, France*
[3]*Carl Zeiss Microscopy GmbH, Carl-Zeiss-Str. 22, 74447 Oberkochen, Germany*
(Received 24 May 2013; published 23 August 2013)

In this joint experimental and theoretical work, we investigate collective electronic excitations (plasmons) in free-standing, single-layer graphene. The energy- and momentum-dependent electron energy-loss function was measured up to 50 eV along two independent in-plane symmetry directions (ΓM and ΓK) over the first Brillouin zone by momentum-resolved electron energy-loss spectroscopy in a transmission electron microscope. We compare our experimental results with corresponding time-dependent density-functional theory calculations. For finite momentum transfers, good agreement with experiments is found if crystal local-field effects are taken into account. In the limit of small and vanishing momentum transfers, we discuss differences between calculations and the experimentally obtained electron energy-loss functions of graphene due to a finite momentum resolution and out-of-plane excitations.

DOI: 10.1103/PhysRevB.88.075433 PACS number(s): 79.20.Uv, 81.05.ue, 73.22.Lp, 71.45.Gm

I. INTRODUCTION

Graphene, with its unique structural and electronic properties, continues to be interesting for fundamental research, while at the same time promising a wide range of applications in fields such as optoelectronics and plasmonics.[1] The promise of graphene-based plasmonic devices[2] has led to increasing interest in the study of plasmons in graphene and their behavior. In general, they can be understood as oscillations of the electron density with a given wavelength (momentum) and frequency (energy). In (doped) graphene, several of these collective electronic excitations exist at different energies: charge-carrier plasmons below 3 eV, the so-called π plasmon at around 5 eV and the $\pi+\sigma$ plasmon at 15 eV.

Experimentally, these excitations and their dispersion, i.e., the relation between energy and momentum, can be probed by electron energy-loss spectroscopy (EELS) or inelastic x-ray scattering (IXS). High-resolution EELS was used extensively to study the plasmon dispersion of epitaxial single-layered and multilayered graphene. The charge-carrier plasmon was investigated for graphene on a variety of different substrates, such as semiconducting SiC (0001),[3–6] metallic Ir (111),[7,8] Pt (111),[9] Ni (111), and Au/Ni (111).[10] Very few studies have reported on the two plasmons at higher energies, e.g., for epitaxial graphene on SiC(0001) (Ref. 5) and Pt(111).[11] IXS measurements of graphite were used to derive the energy-loss function of graphene indirectly.[12] However, in all these cases the influence of the dielectric environment (substrate) has to be taken into account in order to extract information on the intrinsic excitations of graphene. High-energy plasmons in *free-standing* graphene were first studied by scanning transmission electron microscopy (STEM) EELS,[13,14] which has the advantage of a very high spatial resolution, but is restricted to vanishing momentum transfer. So far, experimental results on the momentum-dependent response of free-standing graphene are still incomplete. Our previous work[15] has reported on the dispersion of the π plasmon in free-standing graphene along the ΓM direction up to 0.5 Å^{-1}.

Theoretically, the dielectric response of graphene has been studied extensively by various methods: ranging from simple tight-binding models for the π bands,[16–21] over time-dependent density-functional theory (TDDFT) calculations,[13,22–25] to first-principles calculations that solve the Bethe-Salpeter equation.[26–29] So far, a detailed comparison of the different calculations with experiments is still missing due to the lack of experiments with sufficient energy and momentum resolution: to our knowledge, no direct measurements of the $\pi+\sigma$-plasmon dispersion in free-standing single-layer graphene or the anisotropy of the dielectric response for different in-plane momentum transfers exists.

In this paper, we present direct measurements of the energy-loss function of free-standing, single-layer graphene obtained by momentum-resolved EELS in a transmission electron microscope (TEM). We have measured the electronic response along two nonequivalent symmetry directions (ΓM and ΓK) over the entire first Brillouin zone (see Sec. III A). We compared our results to TDDFT calculations using different approximations (see Sec. III B), specifically the independent-particle approximation (2D-IPA), the random-phase approximation (RPA), and the adiabatic local-density approximation (ALDA) in order to assess the importance of crystal local-field effects and exchange-correlation effects in the loss function of a prototype two-dimensional (2D) material. Significant differences between RPA calculations and experiments are only observed in the limit of vanishing momentum transfers and partially explained by the experimental setup. In particular, we discuss the consequences of a finite momentum resolution (see Sec. III C) as well as contributions of out-of-plane excitations (see Sec. III D).

II. METHODS

A. TEM-EELS experiments

Free-standing, single-layer graphene films were prepared by mechanical exfoliation[30] and transferred to holey carbon grids. We have confirmed the thickness and the absence of contamination by standard high-resolution TEM. EELS investigations were performed on the SALVE I (sub-Angstrom low-voltage electron microscopy) prototype, which is based

 ©2013 American Physical Society

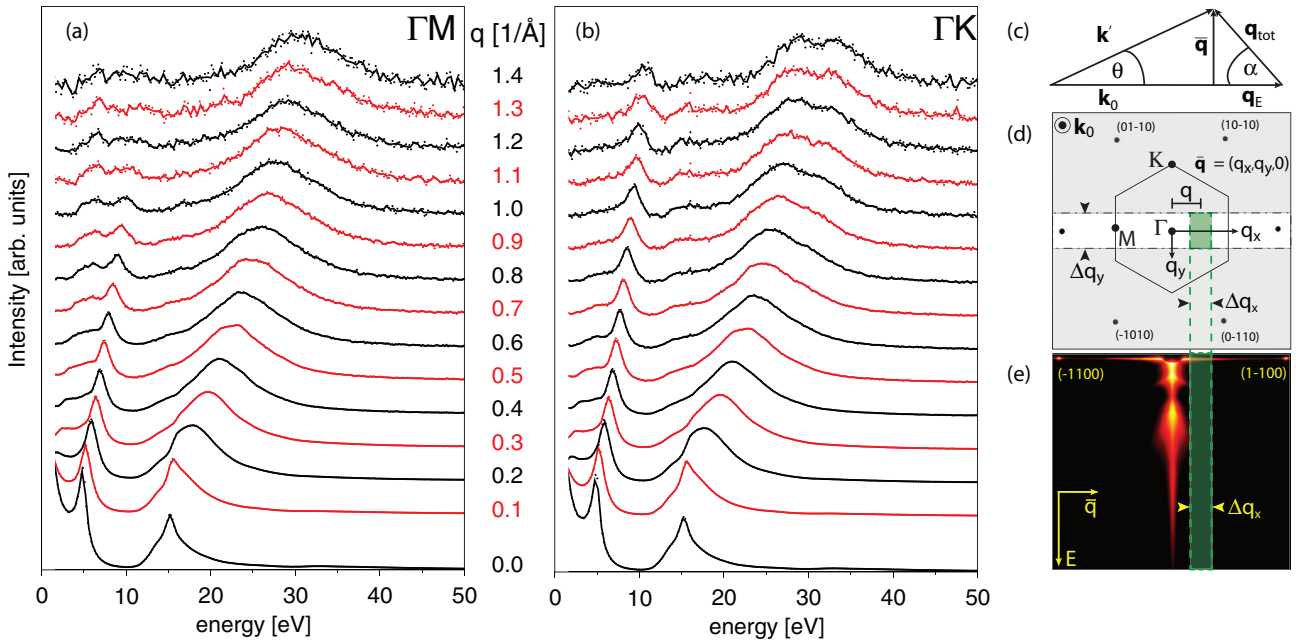

FIG. 1. (Color online) Experimental momentum-dependent energy-loss function of free-standing single-layer graphene along the two nonequivalent symmetry directions ΓM (a) and ΓK (b). The experimental setup is sketched on the right: (c) inelastic scattering geometry in a TEM; (d) electron diffraction pattern of graphene with an illustration of the used (virtual) off-axis aperture geometry; (e) false-color image of a recorded ω-q-map for single-layer graphene. Each line spectrum at position q was extracted by binning (shaded area) over the binning width Δq_x, which corresponds to a (virtual) off-axis aperture $\Delta q_x \times \Delta q_y$ indicated in (d).

on a ZEISS Libra200 TEM and equipped with an in-column Ω filter and monochromator.[31] All spectra in this work were recorded at 40 kV to minimize beam-induced damage. Graphene samples were mounted in a rotation holder.

Intensities measured by TEM-EELS are adequately described by the double-differential scattering cross section,[32] which is directly related to the energy-loss function $-\mathrm{Im}\varepsilon^{-1}(\bar{\boldsymbol{q}},E)$ of the sample by

$$\frac{\partial^2\sigma}{\partial\Omega\,\partial E} \propto \frac{-1}{\bar{q}^2+q_E^2}\mathrm{Im}\,\varepsilon^{-1}(\boldsymbol{q}_{\mathrm{tot}},E). \qquad (1)$$

Here, E is the energy loss of the inelastically scattered electrons and $\boldsymbol{q}_{\mathrm{tot}} = (q_x,q_y,q_E)$ is the total momentum transfer, which can be decomposed into an in-plane component $\bar{\boldsymbol{q}} = (q_x,q_y,0)$ and an out-of-plane component $q_E = E/\hbar v_0$. The latter is associated with the energy loss of the electron and directed along the incident beam, where v_0 is the velocity of the incident electrons ($\approx 0.37c$ at 40 kV). For momentum transfers and energies probed in our experiments, we generally have $q_E \ll q_{\mathrm{tot}}$ and therefore $\boldsymbol{q}_{\mathrm{tot}} \approx \bar{\boldsymbol{q}}$.

We have used the parallel-acquisition EELS mode of the Ω filter[33,34] to record momentum-resolved energy-loss (ω-q) maps as shown Fig. 1(e). For this, the TEM is operated in diffraction mode, where a diffraction pattern is formed in the entrance plane of the Ω filter. Placing a narrow rectangular slit with a slit width $\Delta q_y = 0.25$ Å^{-1} in this plane, we can select electrons that have been scattered along a specific crystallographic direction. The filter disperses these electrons according to their energy perpendicular to the slit axis q_x. Line scans were extracted from these recorded maps by integrating the measured intensity over a binning width $\Delta q_x = 0.1$ Å^{-1}, where the center q of the integrated momentum range indicates the approximate in-plane momentum transfer.

Finally, the experimental energy-loss function $-\mathrm{Im}\varepsilon^{-1}(\bar{\boldsymbol{q}},E)$ was extracted from our raw data by accounting for the Lorentzian scaling factor $(\bar{q}^2+q_E^2)^{-1}$ in Eq. (1). For this, we have adapted the angular correction for a standard EELS geometry[32] to our case of a (virtual) off-axis aperture of size $\Delta q_y \times \Delta q_x$ at position q (for further details, see Supplemental Material[35,36]). The experimental energy resolution was $\Delta E = 0.2$ eV.

B. TDDFT calculations

In order to calculate the energy-loss function $-\mathrm{Im}\varepsilon^{-1}(\bar{\boldsymbol{q}},E)$ of isolated graphene, we have performed first-principles calculations in the framework of time-dependent density-functional theory (TDDFT) using the following four steps (see Ref. 37 for details): (i) First, the Kohn-Sham energies and wave functions are obtained from a self-consistent ground-state calculation with ABINIT.[38] We use the local-density approximation, norm-conserving pseudopotentials,[39] and a plane-wave basis set with energies up to 30 Ha on a $59 \times 59 \times 1$ k-point grid. (ii) Using the DP code,[40] we calculate the Kohn-Sham polarizability χ^0 within linear response. This quantity is found to be converged for small supercells with an interlayer distance d of about 7 Å. (iii) The response of the interacting electrons to an external potential is obtained by solving the Dyson equation $\chi = \chi^0 + \chi^0(v + f_{\mathrm{XC}})\chi$, where v is the Coulomb potential and f_{XC} denotes the exchange-correlation kernel. (iv) Finally, the inverse dielectric function, normalized to the unit area, is given by $\varepsilon^{-1} = 1 + dv\chi$, where d denotes the height of the supercell. (For a stack of repeated graphene layers,

the susceptibility vanishes with increasing interlayer distance $\chi_{GG'} \propto 1/d$.)

In contrast to a standard calculation for a three-dimensional crystal, two numerical difficulties arise due to the localization of the 2D system in the z direction: First, a discrete plane-wave basis set introduces artificial replicas of the sheet which may interact via the long-range Coulomb interaction in step (iii). To avoid this problem, we solve the Dyson equation in a different basis using plane waves $e^{i\bar{\boldsymbol{q}}\bar{\boldsymbol{r}}}$ for the in-plane direction and a real-space grid along the z direction.[41,42] In these mixed coordinates, the Coulomb interaction becomes

$$v(\bar{\boldsymbol{q}},z-z') = \frac{2\pi}{\bar{q}} e^{-|\bar{\boldsymbol{q}}||z-z'|}. \tag{2}$$

Second, the ALDA kernel $f_{\mathrm{XC}}\big[n(\boldsymbol{r})\big]$ diverges for vanishing density $n(\boldsymbol{r})$, i.e., at large distances from the sheet where $\chi^0 \to 0$. To minimize numerical instabilities for the product $\chi^0 f_{\mathrm{XC}}$, we use the same real-space grid along z in the ground-state calculation (i) and for the solution of the Dyson equation (iii) to prevent errors from the Fourier interpolation of $n(\boldsymbol{r})$ on noncompatible grids.

III. RESULTS AND DISCUSSION

A. Experiments

We have measured the energy-loss function of a single, free-standing layer of graphene along the two nonequivalent in-plane momentum directions ΓM and ΓK. The results are plotted in Fig. 1. Looking at $q \to 0$ (bottom), the energy-loss function is dominated by two distinct peaks, located at 4.9 and 15.3 eV. In sp^2-bonded systems, such as graphene or graphite, these peaks are usually associated with collective excitations of the π electrons as well as all (π and σ) valence electrons[13,43] and are labeled π and $\pi+\sigma$ plasmon, respectively. Both plasmon peaks in graphene are significantly red-shifted when compared to the three-dimensional counterpart graphite, where these peaks are found at 7 and 28 eV.[44] Considering peak positions and overall line shape, our experimental findings for $q \to 0$ are in good agreement with reported STEM-EELS measurements.[13,14] With increasing but still small q, both plasmons shift to higher energies. The π plasmon disperses quasilinearly as described in our previous work for ΓM (Ref. 15) and slowly broadens, indicating an increase of Landau damping. This particular plasmon dispersion is a result of strong crystal local-field effects in graphene which mix transitions over a wide range of energies.[22] At $q = 0.4$ Å^{-1}, a weak shoulder between 3 and 5 eV becomes visible. The $\pi+\sigma$ plasmon undergoes similar but more significant changes: With increasing q, the initial triangular-shaped intensity distribution disperses into a much broader and symmetrical peak and the spectral weights are redistributed, changing from a more intense π peak to a stronger $\pi+\sigma$ peak at higher q.

Up to a momentum transfer of $q = 0.5$ Å^{-1}, the loss function of graphene is independent of the crystallographic direction, but becomes anisotropic for larger momentum transfers. For q along ΓM, the observed shoulder between 3 and 5 eV gets more pronounced, eventually developing into a broad feature between 5 and 13 eV, with two distinct peaks. Over the entire measured momentum range, this structure gradually decreases in intensity, almost completely disappearing in spectra above 1.2 Å^{-1}. In contrast, along ΓK we only observe a single dispersing peak, visible up to 1.4 Å^{-1}. In addition, above $q = 0.8$ Å^{-1} we find a pronounced shoulder around 12 eV, not present along ΓM. The shape of the $\pi+\sigma$ plasmon also starts to differ and we observe a splitting of the $\pi+\sigma$ peak into a double-peak structure along ΓK.

Most of the features observed in the loss function of graphene are well known from the study of other sp^2 materials like graphite,[44] carbon nanotubes,[22] as well as hexagonal boron nitride (hBN).[45] In all these materials, the in-plane anisotropy becomes only apparent for excitations with short wavelength (large q). In particular, comparing our experiments on graphene with the loss function of graphite, we find very similar spectra for large momentum transfers $q > 1$ Å^{-1}. Indeed, with decreasing wavelength of the excitations, the Coulomb interaction between neighboring layers in graphite gets smaller [see Eq. (2)] and the graphene layers become almost independent (no screening). It has been shown for graphite that peaks in the loss function at large q are mainly due to interband transitions instead of collective excitations.[43,44] The $\boldsymbol{q}$-dependent splitting of the π peak has been traced back to the anisotropy of Imε (Ref. 43) and explained by the occurrence of different saddle points in the transition energy between the π and π^* bands depending on the in-plane direction of $\boldsymbol{q}$.[44] Also, the double-peak structure of the $\pi+\sigma$ peak in the ΓK direction has been observed in graphite.

B. *Ab initio* calculations

The energy-loss function measured in EELS is directly related to the density response function $\chi = \delta n/\delta V^{\mathrm{ext}}$ which describes the density variation δn of interacting target electrons upon an external perturbation δV^{ext}. In the framework of TDDFT, this quantity can be calculated from the Kohn-Sham polarizability $\chi^0 = \delta n/\delta V^{\mathrm{KS}}$, which describes the linear response of independent Kohn-Sham (KS) particles to changes in the effective potential

$$\delta V^{\mathrm{KS}} = \delta V^{\mathrm{ext}} + \delta V^{\mathrm{H}} + \delta V^{\mathrm{XC}}, \tag{3}$$

i.e., to the external perturbation *plus* the induced variations in the Hartree and exchange-correlation (XC) potential. A relation between χ^0 and χ is obtained by differentiating V^{KS} with respect to n. Several approximations exist for the last two terms in Eq. (3).[37] Here, we consider three common choices with increasing complexity:

2D-IPA. Within the independent-particle approximation, only the macroscopic part of the induced Hartree potential δV_0^{H} is taken into account in addition to the external perturbation. This term represents the Coulomb interaction of electrons in a homogeneous electron gas and gives rise to plasmon excitations. Neglecting also the extension of the charge density perpendicular to the sheet, one can introduce 2D response functions $\bar{\chi}^{(0)}$ which are related by the Dyson equation $\bar{\chi} = \bar{\chi}^0 + \bar{\chi}^0 v_{\mathrm{2D}} \bar{\chi}$, where $v_{\mathrm{2D}} = \frac{2\pi}{q}$ is the effective Coulomb potential in two dimensions.[41] This model of a homogeneous, infinitely thin dielectric layer is generally applied in

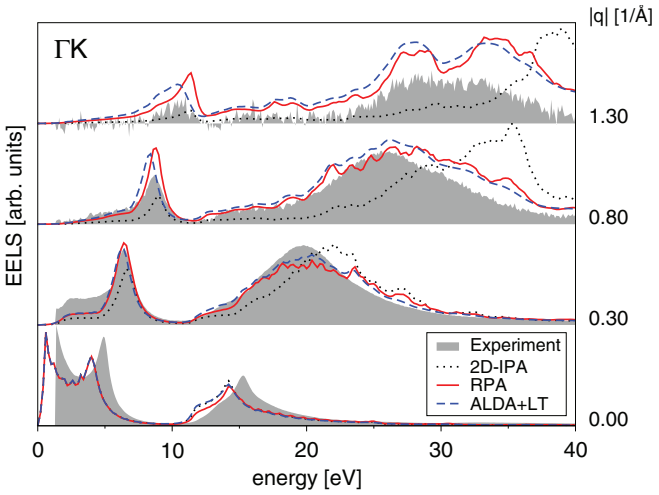

FIG. 2. (Color online) *Ab initio* calculations of the energy-loss function in graphene for different momentum transfers q in the ΓK direction. We compare theoretical results for different approximations (lines, see text for details) with corresponding experimental spectra (shaded area, normalized by a common factor).

tight-binding calculations[19,21,46] or the hydrodynamic description of graphene.[47]

RPA. Within the random-phase approximation, variations in V^{XC} are again neglected, but the layer is now treated as inhomogeneous 3D system, i.e., the induced Hartree potential is fully taken into account including all microscopic contributions $\delta V^{\mathrm{H}}_{\boldsymbol{G}}$. These are the crystal local fields originating from charge fluctuations with high spatial frequency corresponding to a reciprocal lattice vector $\boldsymbol{G}$.[48,49] The Dyson equation then reads as $\chi = \chi^0 + \chi^0 v \chi$, where $\chi^{(0)} \equiv \chi^{(0)}_{\boldsymbol{G}\boldsymbol{G}'}$ are matrices in reciprocal lattice vectors and $v = \frac{4\pi}{|\boldsymbol{q}+\boldsymbol{G}|^2}$ is the 3D Coulomb potential. We include all $\boldsymbol{G}$ up to $G_{\mathrm{cut}} = 8$ Å^{-1} to obtain converged energy-loss spectra.

ALDA + LT. The simplest approximation which partially includes exchange-correlation effects is the adiabatic local-density approximation, where $\delta V^{\mathrm{XC}}(\boldsymbol{r},t)$ is taken from the homogeneous electron gas with density $n(\boldsymbol{r},t)$. Lifetime effects have been included in the calculation of χ^0 following a procedure that was proposed by Mukhopadhyay *et al.*[50] and discussed by others.[51,52] To this end, the quasiparticle lifetime $\tau_{\boldsymbol{k},n}$ has been calculated within the GW approximation for a small set of $\boldsymbol{k}$ points and then roughly fitted in dependence of the energy $E^{\mathrm{LDA}}_{\boldsymbol{k},n}$ for the corresponding KS state of band n (see Supplemental Material[35] for details).

Using our experimental results as a benchmark, we can now assess the importance of crystal local-field effects and exchange-correlation effects for the energy-loss function for this prototype 2D material. Figure 2 shows our TDDFT calculations (lines) in comparison to the normalized measurements (shaded area) for selected in-plane momentum transfers q along the ΓK direction.

In the limit of vanishing momentum transfer $q \to 0$, almost no difference between the three approximations is found (lowest spectra). As in the case of graphite, crystal local-field effects are negligible.[43] However, the energy of the π and $\pi + \sigma$ plasmon at 4.0 and 14.2 eV deviates from the measured peak positions by about 1 eV. It is known from 3D systems that ALDA does not correctly account for exchange-correlation effects for vanishing q and therefore often fails for absorption spectra of extended systems.[37] In 2D systems, where absorption and energy-loss function coincide, we find a similar behavior. Bethe-Salpeter calculations for graphene have shown that XC effects indeed shift the π peak from 4.0 to 4.55 eV.[26] We demonstrate in Sec. III C that also the finite-momentum resolution in the experiment can lead to an apparent energy shift in the loss function.

For finite-momentum transfers $q > 0.2$ Å^{-1}, we obtain very good agreement between RPA calculations (solid lines) and experiment for the momentum-dependent position, width, and intensity of the experimental peaks. Differences at small energies $E < 4$ eV are most probably due to an incomplete subtraction of the zero-loss peak (background from unscattered electrons) in the experimental spectra. Exchange-correlation effects are thus much less important for the loss function of graphene at finite q, which indicates that self-energy effects and the electron-hole interaction just cancel each other like in many 3D systems.[52,53] We also find only very small differences between RPA and ALDA calculations. In contrast, 2D-IPA calculations (dotted lines) strongly deviate with increasing momentum transfer. Two reasons can be given for the failure of 2D-IPA: First, one neglects microscopic inhomogeneities of the charge density, i.e., crystal local-field effects, within the layer. In 3D systems, they influence the loss function only at large $q \gtrsim 1$ Å^{-1} (short wavelength) and shift spectral weight to higher energies.[54] Second, the exponential decay of the Coulomb potential in out-of-plane direction [see Eq. (2)] is ignored in the 2D model of an infinitely thin, homogeneous layer. As a consequence, the effective Coulomb interaction v_{2D} between electrons and thus the plasmon energies are overestimated. The combination of these two points explains the strong difference between 2D-IPA and RPA in graphene when $q > 0.3$ Å^{-1} and the shift of spectral weight to *lower* energies if microscopic components of the induced Hartree potential are taken into account.

At large $q > 1$ Å^{-1}, the double-peak structure of the $\pi + \sigma$ plasmon in the ΓK direction is reproduced qualitatively within the RPA (see top of Fig. 2). However, the exact line shape and intensity deviate from our experimental results. Exchange-correlation effects within the ALDA (dashed lines) shift both plasmon peaks to lower energies and eventually improve the line shape. Lifetime effects, which have been also included in our calculations, remain very small and become only visible at high-energy loss $E > 20$ eV.

For momentum transfers q along the ΓM direction, a very similar behavior is found (see Supplemental Material[35]). The experiments shown in Fig. 1 are in good agreement with our RPA calculations, in particular, we reproduce the isotropy of the dielectric response of graphene for $q < 0.5$ Å^{-1}, the splitting of the π peak at large $q > 0.7$ Å^{-1}, and a single-peak structure for the $\pi + \sigma$ peak. In our ALDA calculations, the line shape is slightly improved, but the peak position is again shifted to energies that are too low by about 0.2 eV. This suggests that exchange-correlation effects beyond the ALDA can be important for a complete understanding of the energy-loss function of graphene at small, finite momentum transfers.

C. Effects of a finite collection aperture

For finite momentum transfers, our calculations reproduce our experimental observations very accurately. The most important differences are found in the limit of $q \to 0$ and can partially be explained by the poor description of XC effects in our calculations. We will demonstrate in the following that a finite width of the collection aperture can also influence peak positions and line shapes in the measured loss function.

The experimental momentum resolution is given by the size of the (virtual) off-axis collection aperture and defined by the slit width Δq_y and binning width Δq_x. This limits the achievable momentum resolution by superimposing the loss functions of adjacent in-plane momentum transfers $\bar{\boldsymbol{q}}$, where two factors influence the weights of the superimposed spectra: (i) The range of contributing momentum transfers and (ii) the Lorentzian intensity distribution of inelastic scattering [prefactor in Eq. (1)], which is relatively steep for small values of $\bar{q}$.

Figure 3 shows the weighted distribution of contributing $|\bar{q}|$ for the present case of a small rectangular (virtual) off-axis collection aperture at three positions q along the slit axis q_x. The weights for a specific $|\bar{q}|$ are given by the product of the arc length of a circle with radius $|\bar{q}|$ truncated by the aperture and the Lorentzian scaling factor $(\bar{q}^2 + q_E^2)^{-1}$ (see Supplemental Material[35,36]). We have plotted the distributions for apertures with a binning width Δq_x of 0.1 and 0.01 Å^{-1}. A slit width Δq_y of 0.25 Å^{-1} was used and q_E was set to 0.006 Å^{-1}, which corresponds to an energy loss of 5 eV for incident electrons with an energy of 40 keV.

For an aperture at position $q = 0$ Å^{-1}, the weighted distributions of $|\bar{q}|$ for both apertures are strongly asymmetric with vanishing contributions at $\bar{q} = 0$ Å^{-1} and a sharp maximum at a finite $\bar{q} \approx 0.008$ Å^{-1}. The asymmetry gradually decreases with increasing q. This behavior is similar for both apertures, however, a smaller binning width Δq_x results in a significantly narrower distribution and therefore an effectively higher momentum resolution, even though the slit width Δq_y is the same in both cases.

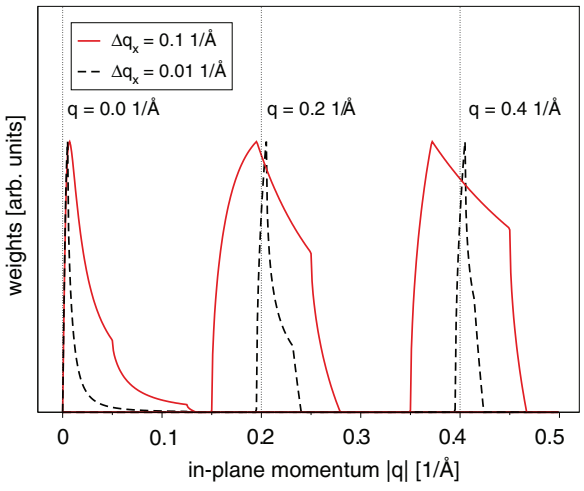

FIG. 3. (Color online) Plot of contributing in-plane momentum transfers $|\bar{q}| = \sqrt{q_x^2 + q_y^2}$ with their corresponding weights for two different-sized (virtual) off-axis apertures: $\Delta q_x = 0.1$ Å^{-1} (solid line) and $\Delta q_x = 0.01$ Å^{-1} (dashed line). We have used the slit width $\Delta q_y = 0.25$ Å^{-1} and $q_E = 0.006$ Å^{-1}. The distributions are plotted at different positions q along the axis q_x. Intensities have been scaled to 1 for all shown curves.

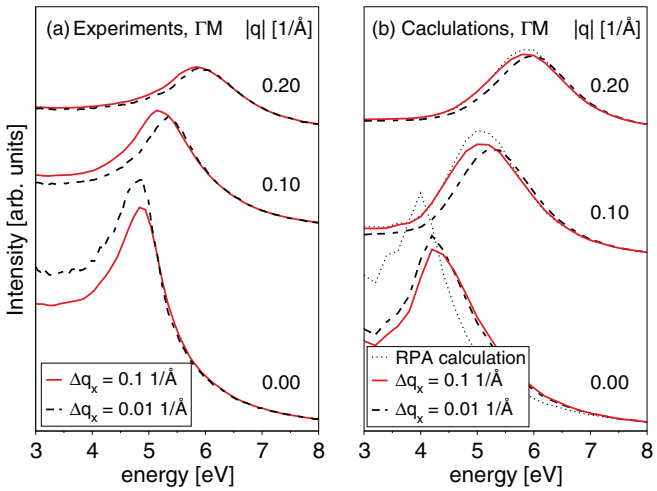

FIG. 4. (Color online) Effect of different-sized collection apertures on the experimental (a) and calculated (b) energy-loss function. Solid lines correspond to $\Delta q_x = 0.1$ Å^{-1} and dashed lines to $\Delta q_x = 0.01$ Å^{-1}. At $q = 0.1$ Å^{-1} a relative shift of the experimental plasmons peaks of 0.2 eV can be observed. This is accurately reproduced by corresponding calculations.

The effect of this finite-momentum resolution on the experimental loss function of graphene is illustrated in Fig. 4(a). Dashed lines correspond to spectra extracted with a binning width Δq_x of 0.1 Å^{-1} and solid lines to 0.01 Å^{-1}. We have focused on the energy-loss region of the π-plasmon peak around 5 eV. At $q = 0$ Å^{-1} a smaller binning width Δq_x results in a marginally reduced plasmon peak width and small changes in intensity, whereas the peak position does not show any significant changes. However, at $q = 0.1$ Å^{-1}, a significant peak shift can be observed. Using a smaller binning width Δq_x, the π-plasmon peak shifts by about 0.2 eV. With increasing q, this shift becomes gradually smaller and vanishes for apertures at positions $q > 0.3$ Å^{-1}.

These findings can be reproduced by including the effect of a finite collection aperture in our TDDFT calculations [see Fig. 4(b) and Supplemental Material[35]). Shown are the corresponding RPA calculations for exact in-plane momentum transfers (dots) as well as the effect of a small (dashed line) and large (solid lines) collection aperture, using the same values for the binning width Δq_x and the slit width Δq_y as before. Comparing the peak positions between the corrected RPA loss functions at $q = 0.1$ Å^{-1}, we observe the same shift of 0.2 eV between the π-plasmon peaks, as seen in the experimental loss function on the left. At $q = 0.2$ Å^{-1}, this shift becomes smaller and vanishes at larger q values. Most notably, at $q = 0$ Å^{-1}, the uncorrected RPA calculations experience a strong blue-shift of 0.25 eV once the effect of a finite collection aperture is taken into account. The observed differences between experiments and RPA calculations of 0.9 eV for the π-plasmon energy at $q = 0$ Å^{-1} can thus be explained as a combination of exchange-correlation effects (0.55 eV) and the effect of the finite collection aperture (0.25 eV).

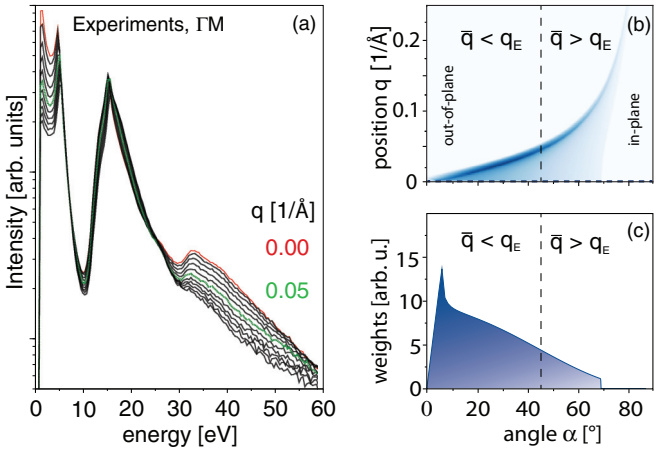

FIG. 5. (Color online) (a) Experimental energy-loss function of graphene along ΓM extracted with a small binning width Δq_x of 0.01 Å^{-1}. Intensities are plotted on a logarithmic scale. A peak between 30 and 45 eV is clearly visible for spectra below $q = 0.1$ Å^{-1}. (b) 2D intensity plot for the weights of contributing q_{tot} with certain angles α at different aperture positions q along the slit axis q_x. (c) Line profile extracted from (b) at position $q = 0$ Å^{-1} for an aperture with a binning width Δq_x of 0.01 Å^{-1}. The majority of contributing momentum transfers q_{tot} are associated with an angle α smaller than 45°.

D. Out-of-plane contributions

We have demonstrated above that the effective momentum resolution strongly depends on the binning width Δq_x. This allows us to investigate the loss function of graphene at very small momentum transfers using a binning width Δq_x of 0.01 Å^{-1}, which corresponds to an effective momentum resolution of approximately 0.03 Å^{-1}. The resulting energy-loss spectra for momentum transfers up to 0.1 Å^{-1} are shown in Fig. 5(a). Apart from small shifts of the π and $\pi + \sigma$ plasmons, we observe an additional feature at 30–45 eV, present along both symmetry directions ΓM and ΓK (not shown). No dispersive behavior is observed and the peak disappears around $q = 0.1$ Å^{-1}. Given an energy loss of 35 eV, the momentum transfer q_E along the incident beam is about 0.05 Å^{-1} and therefore comparable to the in-plane momentum transfers $\bar{q}$ considered here. For values of $\bar{q} < q_E$, the total momentum transfer $\boldsymbol{q}_{\text{tot}}$ is mostly directed out of plane, while for $\bar{q} > q_E$, $\boldsymbol{q}_{\text{tot}}$ quickly becomes orientated parallel to the surface. As the peak at 35 eV is only observed for $\bar{q} < q_E$, we conclude that it is related to the out-of-plane polarization of graphene.

This is further verified by looking at the weighted distribution of angles α (defined in Fig. 1). Figure 5(b) illustrates how the contributions of α change with increasing in-plane momentum transfer q and Fig. 5(c) shows the weighted distributions of α for an aperture placed around $q = 0$ Å^{-1}. For $q = 0$ Å^{-1} the majority of contributing momentum transfers are smaller than q_E. Shifting q away from zero quickly increases the majority of contributing q above q_E. For an aperture placed at $q = 0.1$ Å^{-1}, the main contributions stem from angles between $\alpha = 67°$ and 74°, at $q = 0.2$ Å^{-1} only angles between 78° and 79° contribute.

IV. CONCLUSION

We have presented momentum-resolved electron energy-loss measurements of free-standing, single-layer graphene for momentum transfers along two independent in-plane directions up to the Brillouin-zone boundary. For large $q > 0.5$ Å^{-1}, an anisotropic dielectric response is observed: the π plasmon splits into two peaks along the ΓM direction, while the $\pi + \sigma$ plasmon shows a double-peak structure along ΓK. The high energy and momentum resolution of our experiments made it possible to perform a detailed comparison of experiments with corresponding *ab initio* calculations for this prototype 2D material. At finite momentum transfers, the energy-loss function is found to be very well described within the random-phase approximation, suggesting a cancellation of self-energy effects and electron-hole interaction. Corrections within the adiabatic local-density approximation remain very small as in the case of 3D systems. By contrast, crystal local-field effects become very important due to the finite extension of the charge density along the out-of-plane direction. For $q \to 0$, a very different behavior is observed. Crystal local-field effects and ALDA corrections vanish in this limit, and we find a difference of about 1 eV between calculated and measured plasmon energies. On the one hand, this can be partially understood in terms of strong exchange-correlation effects which already have been discussed for the optical absorption of graphene. On the other hand, we show that the measured plasmon-peak positions can change significantly (by about 0.2 eV) with the size of the applied collection aperture. Further differences between calculations and experiments are observed in the form of an additional feature at higher energy loss and interpreted as out-of-plane excitations of the graphene monolayer.

ACKNOWLEDGMENT

We gratefully acknowledge financial support by the German Research Foundation (DFG) and the Ministry of Science, Research and Arts (MWK) of the state Baden-Württemberg within the sub-Angstrom low-voltage electron microscopy project (SALVE). U.K. and R.H. acknowledge financial support by the DFG under Grant No. KA 1295/18-1.

*philipp.wachsmuth@uni-ulm.de
†Present address: Physics Department, Humboldt-Universität zu Berlin, Zum Großen Windkanal 6, D-12489 Berlin, Germany.

[1] F. Bonaccorso, Z. Sun, T. Hasan, and A. C. Ferrari, Nat. Photonics **4**, 611 (2010).
[2] L. Ju, B. Geng, J. Horng, C. Girit, M. Martin, Z. Hao, H. A. Bechtel, X. Liang, A. Zettl, Y. R. Shen, and F. Wang, Nat. Nanotechnol. **6**, 630 (2011).
[3] Y. Liu, R. F. Willis, K. V. Emtsev, and Th. Seyller, Phys. Rev. B **78**, 201403(R) (2008).
[4] R. J. Koch, T. Seyller, and J. A. Schaefer, Phys. Rev. B **82**, 201413 (2010).
[5] J. Lu, K. P. Loh, H. Huang, W. Chen, and A. T. S. Wee, Phys. Rev. B **80**, 113410 (2009).
[6] C. Tegenkamp, H. Pfnür, T. Langer, J. Baringhaus, and H. W. Schumacher, J. Phys.: Condens. Matter **23**, 012001 (2011).

[7]T. Langer, D. F. Förster, C. Busse, T. Michely, H. Pfnür, and C. Tegenkamp, New J. Phys. **13**, 053006 (2011).
[8]H. Pfnür, T. Langer, J. Baringhaus, and C. Tegenkamp, J. Phys.: Condens. Matter **23**, 112204 (2011).
[9]A. Politano, A. R. Marino, V. Formoso, D. Farías, R. Miranda, and G. Chiarello, Phys. Rev. B **84**, 033401 (2011).
[10]A. Generalov and Y. Dedkov, Carbon **50**, 183 (2012).
[11]A. Politano, A. Marino, V. Formoso, and D. Farías, Plasmonics **7**, 369 (2012).
[12]J. P. Reed, B. Uchoa, Y. I. Joe, Y. Gan, D. Casa, E. Fradkin, and P. Abbamonte, Science **330**, 805 (2010).
[13]T. Eberlein, U. Bangert, R. R. Nair, R. Jones, M. Gass, A. L. Bleloch, K. S. Novoselov, A. Geim, and P. R. Briddon, Phys. Rev. B. **77**, 233406 (2008).
[14]W. Zhou, S. J. Pennycook, and J.-C. Idrobo, Ultramicroscopy **119**, 51 (2012).
[15]M. K. Kinyanjui, C. Kramberger, T. Pichler, J. C. Meyer, P. Wachsmuth, G. Benner, and U. Kaiser, Europhys. Lett. **97**, 57005 (2012).
[16]B. Wunsch, T. Stauber, F. Sols, and F. Guinea, New J. Phys. **8**, 318 (2006).
[17]E. H. Hwang and S. Das Sarma, Phys. Rev. B **75**, 205418 (2007).
[18]A. Hill, S. A. Mikhailov, and K. Ziegler, Europhys. Lett. **87**, 27005 (2009).
[19]Kenneth W.-K. Shung, Phys. Rev. B **34**, 979 (1986).
[20]M. F. Lin, D. S. Chuu, C. S. Huang, Y. K. Lin, and K. W.-K. Shung, Phys. Rev. B **53**, 15493 (1996).
[21]S. Yuan, R. Roldán, and M. I. Katsnelson, Phys. Rev. B **84**, 035439 (2011).
[22]C. Kramberger, R. Hambach, C. Giorgetti, M. H. Rümmeli, M. Knupfer, J. Fink, B. Büchner, L. Reining, E. Einarsson, S. Maruyama, F. Sottile, K. Hannewald, V. Olevano, A. G. Marinopoulos, and T. Pichler, Phys. Rev. Lett. **100**, 196803 (2008).
[23]J. Yan, K. S. Thygesen, and K. W. Jacobsen, Phys. Rev. Lett. **106**, 146803 (2011).
[24]V. Despoja, D. Novko, K. Dekanić, M. Šunjić, and L. Marušić, Phys. Rev. B. **87**, 075447 (2013).
[25]Y. Gao and Z. Yuan, Solid State Commun. **151**, 1009 (2011).
[26]L. Yang, J. Deslippe, C.-H. Park, M. L. Cohen, and S. G. Louie, Phys. Rev. Lett. **103**, 186802 (2009).
[27]L. Yang, Phys. Rev. B **83**, 085405 (2011).
[28]Z. Chen and X.-Q. Wang, Phys. Rev. B **83**, 081405(R) (2011).
[29]P. E. Trevisanutto, M. Holzmann, M. Côté, and V. Olevano, Phys. Rev. B **81**, 121405 (2010).
[30]J. C. Meyer, C. O. Girit, M. F. Crommie, and A. Zettl, App. Phys. Lett. **92**, 123110 (2008).
[31]U. Kaiser, J. Biskupek, J. Meyer, J. Leschner, L. Lechner, H. Rose, M. Stöger-Pollach, A. Khlobystov, P. Hartel, H. Müller, M. Haider, S. Eyhusen, and G. Benner, Ultramicroscopy **111**, 1246 (2011).
[32]R. Egerton, *Electron Energy-Loss Spectroscopy in the Electron Microscope*, 3rd ed. (Springer, Berlin, 2011).
[33]L. Reimer, I. Fromm, and R. Rennekamp, Ultramicroscopy **24**, 339 (1988).
[34]L. Reimer and R. Rennekamp, Ultramicroscopy **28**, 258 (1989).
[35]See Supplemental Material at http://link.aps.org/supplemental/10.1103/PhysRevB.88.075433 for details on the experimental and numerical methods.
[36]The code for calculating the momentum distribution is available at https://github.com/rhambach/TEMareels.
[37]S. Botti, A. Schindlmayr, R. D. Sole, and L. Reining, Rep. Prog. Phys. **70**, 357 (2007).
[38]X. Gonze, G. M. Rignanese, M. Verstraete, J. M. Beuken, Y. Pouillon, R. Caracas, F. Jollet, M. Torrent, G. Zerah, M. Mikami, P. Ghosez, M. Veithen, J. Y. Raty, V. Olevano, F. Bruneval, L. Reining, R. W. Godby, G. Onida, D. R. Hamann, and D. C. Allan, Z. Kristallogr. **220**, 558 (2005).
[39]N. Troullier and J. L. Martins, Phys. Rev. B **43**, 1993 (1991).
[40]V. Olevano, L. Reining, and F. Sottile, http://www.dp-code.org.
[41]R. Hambach, Ph.D. thesis, Ecole Polytechnique, 2010.
[42]Z. Yuan and S. Gao, Comput. Phys. Commun. **180**, 466 (2009).
[43]A. G. Marinopoulos, L. Reining, A. Rubio, and V. Olevano, Phys. Rev. B **69**, 245419 (2004).
[44]K. Zeppenfeld, Z. Phys. **243**, 229 (1971).
[45]S. Galambosi, L. Wirtz, J. A. Soininen, J. Serrano, A. Marini, K. Watanabe, T. Taniguchi, S. Huotari, A. Rubio, and K. Hämäläinen, Phys. Rev. B. **83**, 081413 (2011).
[46]T. Stauber, J. Schliemann, and N. M. R. Peres, Phys. Rev. B **81**, 085409 (2010).
[47]V. B. Jovanović, I. Radović, D. Borka, and Z. L. Mišković, Phys. Rev. B **84**, 155416 (2011).
[48]S. L. Adler, Phys. Rev. **126**, 413 (1962).
[49]N. Wiser, Phys. Rev. **129**, 62 (1963).
[50]G. Mukhopadhyay, R. K. Kalia, and K. S. Singwi, Phys. Rev. Lett. **34**, 950 (1975).
[51]S. Rahman and G. Vignale, Phys. Rev. B **30**, 6951 (1984).
[52]H.-C. Weissker, J. Serrano, S. Huotari, E. Luppi, M. Cazzaniga, F. Bruneval, F. Sottile, G. Monaco, V. Olevano, and L. Reining, Phys. Rev. B **81**, 085104 (2010).
[53]G. Onida, L. Reining, and A. Rubio, Rev. Mod. Phys. **74**, 601 (2002).
[54]S. Waidmann, M. Knupfer, B. Arnold, J. Fink, A. Fleszar, and W. Hanke, Phys. Rev. B **61**, 10149 (2000).